Journal of Visualization, Vol. 10, No. 3 (2007)317-324

**Regular Paper**

# Self-Induced Rotary Sloshing Caused by an Upward Round Jet in a Cylindrical Container

Ueda, Y.*[1], Hayashida, Y.*[1], Iguchi, M.*[1] and Ishii, T.*[2]

*1 Division of Materials Science and Engineering, Graduate School of Engineering, Hokkaido University, Nishi 8, Kita 13, Kita-Ku, Sapporo, Hokkaido 060-8628, Japan. E-mail: y-ueda@eng.hokudai.ac.jp
*2 JFE R&D Corporation, 1-1 Minami-Watarida-Cho, Kawasaki-Ku, Kawasaki, Kanagawa 210-0855, Japan.

Received 5 January 2007
Revised 11 June 2007

***Abstract*** : Jet-induced rotary sloshing of a Newtonian fluid in a partially filled cylindrical container is numerically and experimentally visualized to investigate a flow pattern inside the rotary sloshing wave. Visualization techniques employed in this study include Computational Fluid Dynamics (CFD) and Particle Image Velocimetry (PIV). Result for the sloshing period is compared with the theoretical result of a small time-harmonic irrotational flow of an inviscid and incompressible fluid, and several results for 3D view of the rotary sloshing and the velocity vector in the vertical and horizontal cross-sections are given.

***Keywords*** : Self-induced sloshing, Rotary sloshing, Cylindrical tank, Round jet, PIV, CFD.

## 1. Introduction

We consider rotary sloshing of a Newtonian fluid in a partially filled cylindrical container. The sloshing of fuel tank in an aircraft or ship could affect the performance of the control systems and so it is desirable to avoid external vibration at the eigenfrequency of the liquid. Therefore, several authors have addressed this issue, starting with the pioneering work of Lamb (1932). Analytically, the sloshing problem may be treated as follows (see Lamb, 1932; Ibrahim, 2005; Ueda et al., 2007). The velocity potential, $\phi$, for the small amplitude of an inviscid, incompressible fluid must satisfy the Laplace equation in the fluid domain, have zero normal derivative at the solid walls of the container and satisfy the linearized free-surface condition (Assumed that surface tension would be negligible). The harmonic solution of the Laplace equation provides the frequency of the counter-clockwise rotary sloshing wave, $\omega_i$, which is described as

$$\omega_i = \frac{2\pi}{T_i} = \sqrt{\frac{2gk_i}{D}\tanh\left(\frac{2k_iH_L}{D}\right)}. \tag{1}$$

where $T_i$ is a period of the sloshing, $H_L$ is a static liquid level, $D$ is the diameter of the container, $g$ is the acceleration due to gravity and $k_i$ is the $i$th root of the derivative of the first-order Bessel function, $J_1'(k_i)$, and for example, the value of $k_1$ is approximately 1.84118.

Self-induced sloshing is observed in the liquid in the partially filled container having an inlet jet and a drain nozzle. The inlet jet is injected through the inlet nozzle and the same quantity is synchronously drained through the outlet pipe so that the liquid volume in the bath is kept in constant. The inlet jet impinges on the free surface and then a surface swell is formed. After the jet is injected pressure fluctuation generated by the surface swell results in the periodical oscillating motion (sloshing). For more detailed knowledge one may cite a series of articles by Madarame's group (see, for instance, Madarame et al., 2002). They experimentally investigated the possible sloshing mode and the energy supply mechanism between the

displacement of the inlet jet and the rotary sloshing wave.

The associated rotary sloshing has been utilized in some industrial fields, for example, a snow melting system (see Iguchi et al., 2002) and an organic wastewater disposal facility (see Shitara et al., 2003). In these applications the injected liquid jet is replaced by a bubble or ozone-air mixture jet and the rotary sloshing plays a key role in accelerating chemical reaction.

The target flow in this study is the self-induced rotary sloshing. The visualization techniques used in this study include the Experimental and Computational Fluid Dynamics (EFD and CFD). Particle Image Velocimetry (PIV) system was employed to experimentally visualize these parts of the flow. FLUENT™, a commercially available CFD software package, was employed to simulate these flows. In order to check the accuracy of the employed CFD technique, a comparative study of the PIV measurement on the same flow was conducted in this paper. The swirl period and coloured jet behaviour were experimentally measured and compared with a theoretical result. An internal flow pattern was visualized, and a velocity profile due to the rotary sloshing and inlet jet was discussed.

# 2. Experimental Setup and Procedure

## *2.1 Test Apparatus and Operating Condition*

Experimental apparatus is shown in Fig. 1. A transparent cylindrical container having an inner diameter of 200 mm consists of an inlet pipe ($13^{\phi}$ mm) and two outlet pipes ($18^{\phi}$ mm each). The inlet pipe is set at the centre of the container bottom and the outlet pipes are both set at 75 mm from the centre. The cylindrical container is surrounded by a larger acrylic rectangular tank. Ionic water is immersed in the rectangular container so that no distortion appears in a photograph. The inlet round jet was injected into the bath through the inlet pipe and the flow rate was controlled by a pump. The same quantity as the inlet jet was drained through two outlet pipes so that the water in the bath was kept at a specified volume. The inlet velocity of the jet was measured based upon the flow rate by a flow meter. The aspect ratio, $\mathscr{A}$, defined by the water level-to-container diameter, $H_L/D$, was varied in the range $0.3 \leqslant \mathscr{A} \leqslant 1.7$. In the outside of the range the swirl motion was no longer observed. The flow rate of the inlet jet, $Q_L$, was also varied in the range $2.2 \times 10^{-4} \leqslant Q_L \leqslant 4.0 \times 10^{-4}$ m³/s.

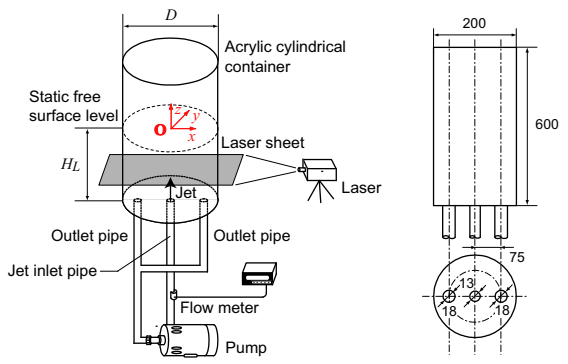


Fig. 1. Sketch of experimental apparatus (units in mm).

## *2.2 PIV Measurement*

The swirling flow pattern in the vertical or horizontal cross-section and the vertical velocity were obtained by use of a PIV system consisting of a double-pulsed laser, laser sheet optics, charge-coupled device (CCD) camera, timing circuit, image-sampling computer and image-processing software (ILA GmbH/OFS Ltd., FLOW DIAGNOSTIC_SOFTWARE). The double-pulsed laser (BIG SKY LASER TECHNOLOGIES, Inc., Model ULTRA) is a combination of a pair of Nd-YAG lasers, each having an output of 33 mJ/pulse and a pulse width-FWHM of 6.8 nsec. The timing circuit communicates with the CCD camera and computer and generates pulses to control the double-pulsed laser. The CCD camera used (Redlake MASD, Inc., MEGAPlus Camera, Model ES 1.0) has a pixel clock rate of 20 MHz and a frame rate of 30 fps (dual channel mode) and 15 fps (single channel mode).

The vertical cross-section of the swirling flow was illuminated by the double-pulsed laser for measurement of the circulation flow pattern. The horizontal cross-section was also measured by illuminating the horizontal planes perpendicular to the vertical plane. The tracer particles used to seed the flow are a vinylidene chloride-acrylonitrile copolymer 20-30 μm in diameter and the specific gravity of approximately 1.05. The particle concentration of $1.2 \times 10^{-2}$ g/L was adjusted so that on average at least ten particle pairs were observed in an interrogation window for each case. Other PIV papers were found in Watanabe et al. (2005) and Ramesh et al. (2006).

### *2.3 Inlet Jet Visualization*

The jet behaviour was visualized using a fluorescence dye, Rhodamine B ($C_{28}H_{31}ClN_2O_3$). Rhodamine B was injected into the bath through the inlet nozzle when the rotary sloshing would stably appeared. Photograph of an instantaneous coloured jet behaviour was taken by the CCD video camera in the longitudinal view.

## 3. Computational Procedure

The FLUENT numerical code, version 6.2.16, was employed for all numerical predictions on 2.8 GHz Pentium IV processor with 1 GB RAM. GAMBIT 2.2.30 was used for the establishment of the three-dimensional computational grid.

The computational grid was employed in the present study, which was based upon an actual container geometry and the geometric information given in Fig. 1. The grids were made up of hexahedral elements and a total of 109,690 cells was employed for entire flow domain.

FLUENT uses a control-volume-based technique to solve the governing continuity and momentum equations. A segregated implicit solver and second-order upwind interpolation scheme were employed for each computational iteration, as these provided accurate predictions of the jet-induced sloshing within water/air two-phase flow. A small time-step size, $\Delta t = 2.5 \times 10^{-3}$ s, was adopted to achieve convergence in every time step. Free surface behaviour is tracked by the Volume-of-Fluid (VOF) model (Geo-Reconstruct). The tracking of the interface between the phases is accomplished by the solution of a continuity equation for the volume fraction of a phase. The Large Eddy Simulation (LES) model was selected because of a direct resolution of the large-scale eddies. The large-scale eddies are solved explicitly by the filtered Navier-Stokes equations, and the small eddies are modeled using a sub-grid scale (SGS) model. In Smagorinsky-Lilly model, the eddy-viscosity is modeled by $\mu_t = \rho L_s^2 |\bar{\mathbf{S}}|$ where $L_s$ is the mixing length for subgrid scales and $|\bar{\mathbf{S}}| := \sqrt{2\bar{S}_{ij}\bar{S}_{ij}}$. In FLUENT code $L_s$ is computed by $L_s = \min(\kappa d_1, C_s V^{1/3})$ where $\kappa$ is the Kármán constant, $d_1$ is the distance to the closest wall, $V$ is the volume of the computational cell, and $C_s$ is the Smagorinsky constant and the default value of $C_s$ adopted by the FLUENT code is 0.1. The convergence of the computational solution was determined based upon residuals for the continuity and $x$-, $y$-, $z$-velocities. The residual of all quantities was set to $10^{-4}$. The solution was considered to be converged when all of the residuals were less than or equal to these default settings (see FLUENT 6.2 User's Guide for more details).

## 4. Results and Discussion

### *4.1 Sloshing Period and Jet Streakline*

We first measured the sloshing period when the rotary sloshing stably appeared. This quantity makes it possible to check the accuracy of the employed procedure against the theoretical prediction of Eq. (1). Figure 2 shows a comparison of the computed and experimentally measured swirl periods. The period, $T$, and the water depth, $H_L$, are normalized by $\sqrt{D/g}$ and the diameter of the container, $D$, respectively. As observed, the computed and experimentally measured periods are nicely obtained. By using the velocity potential of the small time-harmonic irrotational sloshing motion, Madarame et al. (2002) proposed a simple physical

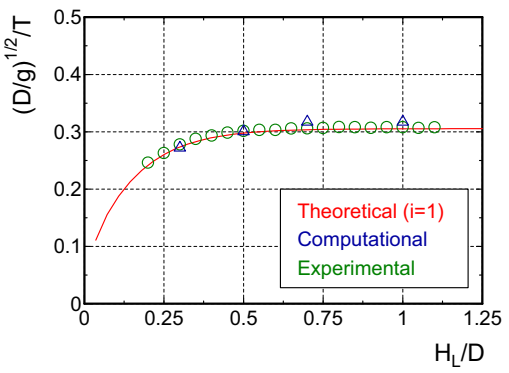


Fig. 2. Aspect ratio versus swirl period for $Q_L = 2.6 \times 10^{-4}$ m$^3$/s in different approaches.

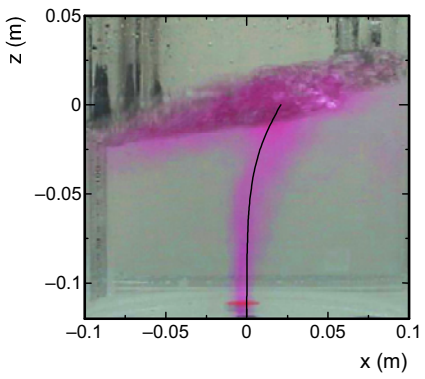


Fig. 3. Jet streakline for $Q_L = 2.6 \times 10^{-4}$ m$^3$/s and $\mathscr{A} = 0.6$. Solid line exhibits a simple physical prediction of Madarame et al. (2002).

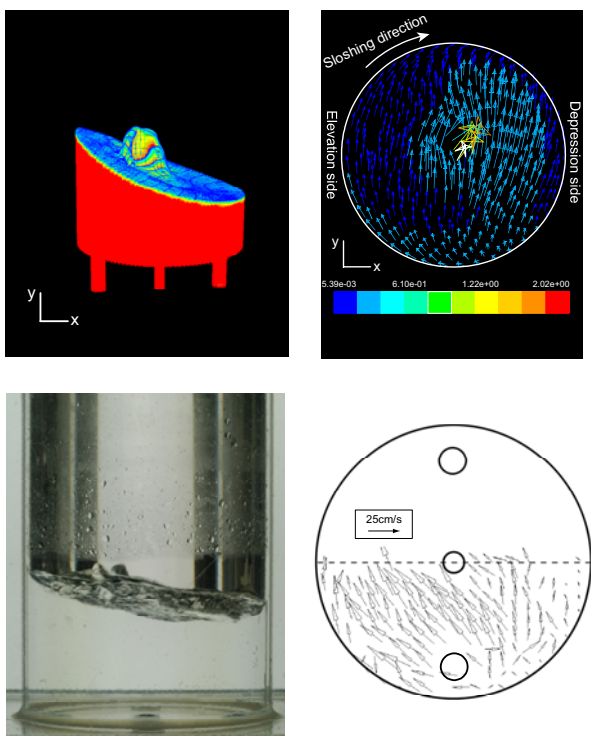


Fig. 4. Comparison of computed (top) and experimental (bottom) flow patterns for $\mathscr{A} = 0.5$ and $Q_L = 2.6 \times 10^{-4}$ m$^3$/s. (Left): 3D view of the swirl motion; (right): velocity vector in the horizontal cross-section at $z = -0.05$ m.

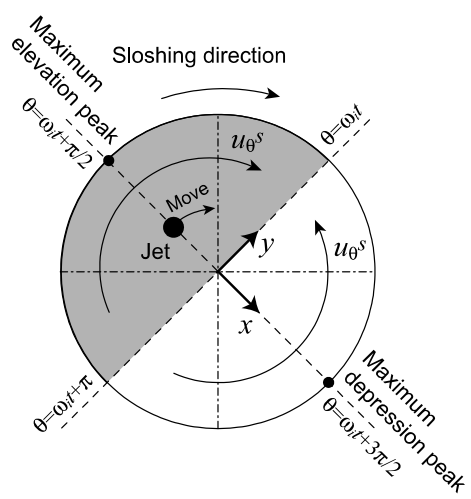


Fig. 5. Schematic of the instantaneous flow pattern in the horizontal cross-section. The elevation of the free surface is positive in the shaded area.

model of the inlet jet streakline. The lateral displacement of the jet from the vertical axis is described by Eqs. (3)-(8) of their paper. Figure 3 shows the trajectory of the coloured inlet jet for $Q_L = 2.6 \times 10^{-4}$ m$^3$/s and $\mathscr{A} = 0.6$. To evaluate the small amplitude solution the computed jet streakline is depicted on the same photograph. Note that the amplitude, $A$, was used in the measured value of $3.35 \times 10^{-2}$ m. The computed jet streakline seems to be almost in agreement with the experimental coloured jet behaviour. In the actual experiment it was observed that the inlet jet inclines to the elevation side of the sloshing wave and rotates in the same direction as the rotary sloshing wave (see Figs. 3 and 5).

### *4.2 Comparison of Flow Pattern between Jet-Induced and Pure Rotary Sloshings*

In Fig. 4 the selected comparison of the computed and experimental (PIV) flow patterns is presented for $Q_L = 2.6 \times 10^{-4}$ m$^3$/s and $\mathscr{A} = 0.5$. The left side of Fig. 4 is the 3D view of the sloshing, and the right side is the velocity vector in the horizontal cross-section at $z = -0.05$ m. It may be seen that the computation (top side of Fig. 4) is virtually identical with the experimental flow visualization (bottom side of Fig. 4)*. In computation the amplitude of the sloshing exhibits the value of $3.47 \times 10^{-2}$ m, which is almost close to the experimentally measured value of $3.5 \times 10^{-2}$ m. Ueda et al. (2007) displays the velocity potential, $\phi^s$, of the small time-harmonic first-mode rotary sloshing of the inviscid and incompressible fluid in the cylindrical container. The tangential velocity, $u_\theta^s = (1/r)(\partial\phi^s/\partial\theta)$, and the vertical velocity, $u_z^s = (\partial\phi^s/\partial z)$, at any point $\boldsymbol{x}$ and the elevation of the free surface, $\eta = -(1/g)(\partial\phi^s/\partial t)_{z=0}$, are then calculated as

$$u_\theta^s(r,\theta,z;t) = \frac{Ag}{r}\frac{J_1(k_i r/a)}{\omega_i |J_1(k_i)| \cosh(k_i H_L/a)} \cosh[k_i(z+H_L)/a] \sin(\theta - \omega_i t), \tag{2}$$

*Although the surface wave of the experimental photograph might seem to be a little fluctuated, the higher modes of the surface wave are actually vanishingly small under the stable condition of $\mathscr{A} = 0.5$ and, therefore, the measured sloshing periods of Fig. 2 are in good agreement with the first mode of the theoretical solution (solid line of Fig. 2). One can cite the related issue in Yoshida et al. (2003).

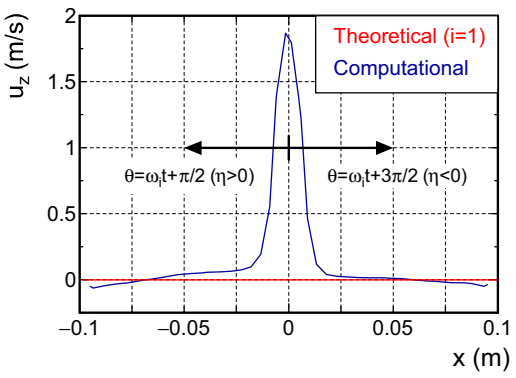


Fig. 6. Vertical component of velocity, $u_z$, on $x$-axis at $z = -0.06$ m. The coordinate system is shown in Figs. 1, 4 and 5.

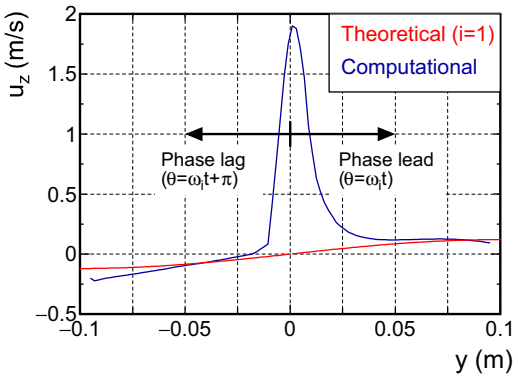


Fig. 7. Vertical component of velocity, $u_z$, on $y$-axis at $z = -0.06$ m. The coordinate system is shown in Figs. 1, 4 and 5.

$$u_z^s(r,\theta,z;t) = -\frac{Ag}{a}\frac{k_i J_1(k_i r/a)}{\omega_i |J_1(k_i)| \cosh(k_i H_L/a)} \sinh[k_i(z+H_L)/a] \cos(\theta - \omega_i t), \tag{3}$$

$$\eta(r,\theta;t) = \frac{AJ_1(k_i r/a)}{|J_1(k_i)|} \sin(\theta - \omega_i t), \tag{4}$$

where $a$ is the radius of the cylindrical container and $\omega_i$ is the angular velocity of Eq. (1). Figure 5 shows a schematic of the flow pattern in the horizontal cross-section. At time $t$, the maximum elevation (or depression) peak is found to be at $\theta = \omega_i t + \pi/2$ (or $\theta = \omega_i t + 3\pi/2$), and the elevation of the free surface, $\eta$, is positive (or negative) for $\omega_i t \leqslant \theta \leqslant \omega_i t + \pi$ (or $\omega_i t + \pi \leqslant \theta \leqslant \omega_i t + 2\pi$). Equation (2) exhibits the negative tangential velocity for $\omega_i t \leqslant \theta \leqslant \omega_i t + \pi$ and the positive tangential velocity for $\omega_i t + \pi \leqslant \theta \leqslant \omega_i t + 2\pi$. We notice that the sloshing wave is rotating in the clockwise direction. This flow pattern is found to be identical with the CFD and PIV results shown in Fig. 4.

Figures 6 and 7 show the vertical components of velocity, $u_z$, on the $x$- and $y$-axes at $z = -0.06$ m. Theoretical results of Eq. (3) are coloured in red and the CFD results are in blue. We notice that the coordinate system is shown in Figs. 4 and 5. The theoretical velocity, $u_z^s$, becomes zero on the $x$-axis because of $\cos(\theta - \omega_i t) = 0$ at $\theta - \omega_i t = \pm\pi/2$. On the $y$-axis the theoretical velocity, $u_z^s$, is positive for $\theta - \omega_i t = 0$ (on $y > 0$ side) or negative for $\theta - \omega_i t = \pi$ (on $y < 0$ side). In the present rotary sloshing, the effect of the higher frequency for $i \geqslant 2$ was observed to be sufficiently small, and therefore the lowest root (first mode) of $k_1 = 1.84118$ was taken in the calculation of Eq. (3). It may be seen that these velocity profiles are almost in agreement with the CFD results of the jet-induced rotary sloshing except for the core region of the inlet jet, $|x| \lessapprox \pm 0.025$ m.

Figure 8 shows the free surface shape and the velocity vector on the elevation (top side) and depression (bottom side) sides of the free surface for $\mathscr{A} = 0.5$ and $Q_L = 2.6 \times 10^{-4}$ m³/s†. The left side of Fig. 8 is the CFD results and the right side is the PIV results‡. For easy to view, the vector plots larger than 0.6 m/s in the CFD result and 0.348 m/s in the PIV results are discarded. The swirl direction of the rotary sloshing and the coordinate system are also inscribed in these figures. In addition, the velocity vector is calculated in the vertical cross-section at $x = -0.07$ m (top side) and $x = 0.07$ m (bottom side). At this time the maximum elevation peak of the free surface is exactly at $(x, y) = (-0.1\,\text{m}, 0.0\,\text{m})$. We observe that the $z$-component of the velocity is positive (or negative) on the phase lead (or lag) side of the maximum elevation of the free surface. On the other hand, the $z$-component of the velocity seems to be negative (or positive) on the phase lead (or lag) side of the maximum depression of the free surface. Figure 9 shows the tangential velocity, $u_\theta$, on the white line of Fig. 8 (left), that is, on

†In a preliminary experiment we have confirmed the periodicity of the rotary sloshing and checked the higher flow rate condition. It seemed that the global characteristics of these flow patterns are almost identical with a single pair of the CFD and PIV results, shown in Figs. 4 and 8, under the stable (lowest mode) sloshing condition.

‡The CCD camera equipped with the PIV system which we employed in this study has a frame rate of 30 fps and, therefore, the snapshots is taken every 0.033 s. As we already mentioned in Section 4.1, the sloshing period is about 0.4797 s for $\mathscr{A} = 0.5$ so that about 14 sheets of the snapshots are taken over one cycle of the sloshing. The 14 snapshots per one period are thought not to be sufficient and, therefore, it is difficult to exactly obtain the same free surface condition as the CFD results. In Fig. 8 we selected the best result in some sets of the experiment.

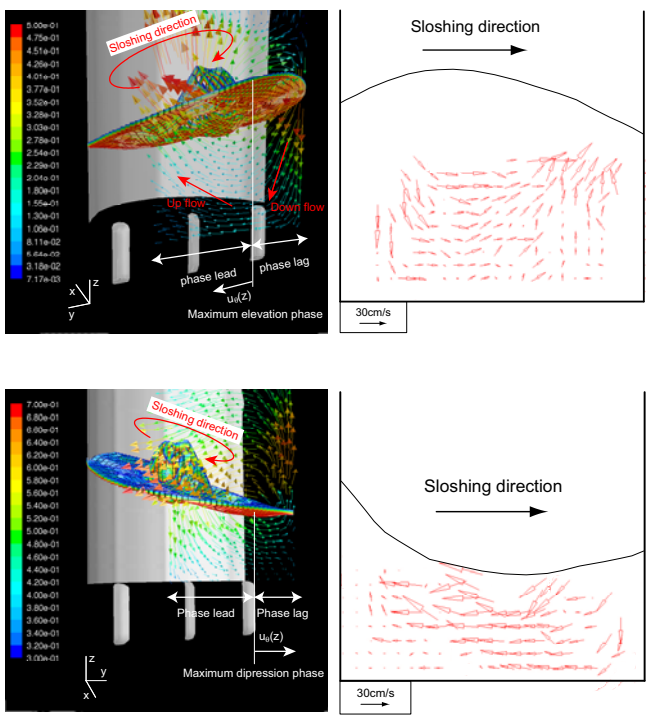


Fig. 8. Comparison of a flow pattern between elevation (top) and depression (bottom) sides for $\mathscr{A} = 0.5$ and $Q_L = 2.6 \times 10^{-4}$ m$^3$/s in the vertical cross-section at $x = -0.07$ m (top) and $x = 0.07$ m (bottom). (Left): CFD results; (right): PIV results.

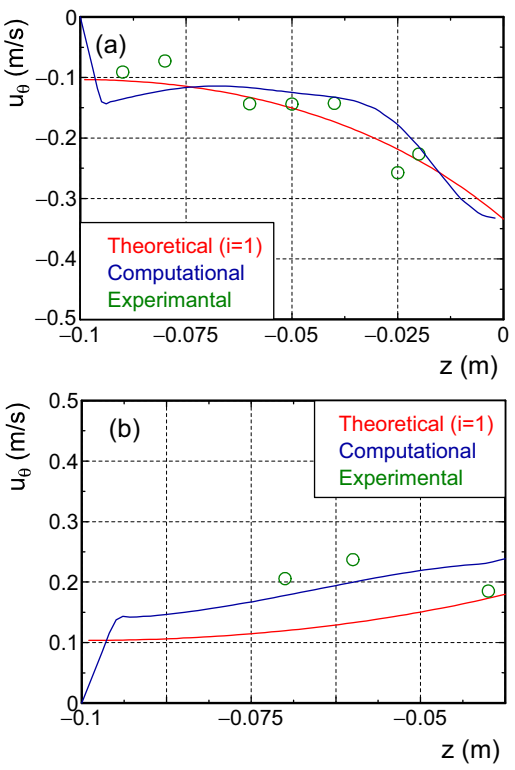


Fig. 9. Tangential component of velocity, $u_\theta$, versus position $z$ for $\mathscr{A} = 0.5$ and $Q_L = 2.6 \times 10^{-4}$ m$^3$/s at (a) $x = -0.07$ m (elevation side); (b) $x = 0.07$ m (depression side). The coordinate system is shown in Fig. 8.

the line of $(-0.07\,\mathrm{m}, 0.0\,\mathrm{m}, -0.1\,\mathrm{m})$–$(-0.07\,\mathrm{m}, 0.0\,\mathrm{m}, 0.0\,\mathrm{m})$ and $(0.07\,\mathrm{m}, 0.0\,\mathrm{m}, -0.1\,\mathrm{m})$–$(0.07\,\mathrm{m}, 0.0\,\mathrm{m}, -0.025\,\mathrm{m})$. Theoretical result of Eq. (2) is coloured in red, the CFD result in blue and the experimental result in green. The measured value of the amplitude, $A = 3.5 \times 10^{-2}$ m, was used in the calculation of Eq. (2). The theoretical results of Eqs. (2)-(4) are based upon the potential flow and hence it is no longer valid inside the boundary layer on the bottom wall of the container (near $z = -0.1$ m). On the elevation side of the free surface (Fig. 9 (a)), the tangential velocity profile, $u_\theta$, seems to be almost identical except inside the boundary layer. According to Eq. (2), the magnitude of the inviscid sloshing solution, $|u^s_\theta|$, is identical between both sides of $0 \leqslant \theta - \omega_i t \leqslant \pi$ ($\eta > 0$) and $\pi \leqslant \theta - \omega_i t \leqslant 2\pi$ ($\eta < 0$). Unlike the pure rotary sloshing of Eq. (2) the present target flow is the jet-induced rotary sloshing. The inlet jet could affect the velocity field so that the magnitude of the tangential velocity, $|u_\theta|$, is expected to be different between both sides of $\eta > 0$ and $\eta < 0$. Indeed, it seems that $u_\theta$ is larger on $\eta < 0$ side than on $\eta > 0$ side in Fig. 9.

### *4.3 Two-Dimensional Effect of Inlet Jet in a Horizontal Plane*

Within the potential flow theory, a fundamental contribution due to the inlet jet is modelized by a series of vortex ring, that is, the doublet in the horizontal cross-section[§]. The velocity potential, $\phi^s$, for the small amplitude of the 1st mode rotary sloshing can be written by the Laplace equation, $\nabla^2 \phi^s = 0$. We note that $\phi^s$ is displayed in Ueda et al. (2007). Introducing a new perturbation parameter $\epsilon := \sqrt{a/H_L} \prec 1$ and an inner variable $\hat{z}$ such that $\hat{z} = \epsilon z = O(1)$, the 3D Laplace equation asymptotically becomes

$$\frac{\partial^2 \Phi}{\partial r^2} + \frac{1}{r}\frac{\partial \Phi}{\partial r} + \frac{1}{r^2}\frac{\partial^2 \Phi}{\partial \theta^2} = -\epsilon^2 \frac{\partial^2 \Phi}{\partial \hat{z}^2}. \tag{5}$$

The assumption of $\epsilon \prec 1$ implies that the fluid flow in the $z$-direction would be negligible and hence it is possible to handle the sloshing motion in 2D. Using the asymptotic series of $\Phi = \Phi_0 + \epsilon^2 \Phi_1 + O(\epsilon^4)$ such

[§]A jet flow is often simulated by a series of vortex rings (see, Cortelezzi & Karagozian, 2001). Since the diameter of the container, $D$, is much larger than the diameter of the inlet nozzle, $d$, the induced velocity by the vortex ring is represented by the doublet (see, Pozrikidis, 1997).

Table 1. $u_\theta^s$ versus $u_\theta^j$ at $|x| = 0.07$ m for $A = 3.5 \times 10^{-2}$ m, $Q_L = 2.6 \times 10^{-4}$ m$^3$/s and $\mathscr{A} = 0.5$.

| $z$ m | $\lvert u_\theta^s \rvert$ m/s at $\theta = \pm\pi/2$ | $\lvert u_\theta^j \rvert$ m/s at $\theta = \pm\pi/2$ |
|---|---|---|
| $-0.09$ | 0.019 | $3.312 \times 10^{-5}$ |
| $-0.07$ | 0.060 | $1.154 \times 10^{-5}$ |
| $-0.05$ | 0.109 | $3.127 \times 10^{-6}$ |

that $\Phi_n = \Phi_{n0} + \epsilon\Phi_{n1} + \cdots$ and $\Phi_{n0}, \Phi_{n1} = O(1)$, the velocity potential is found, from Eq. (5), to obey

$$\frac{\partial^2\Phi_0}{\partial r^2} + \frac{1}{r}\frac{\partial\Phi_0}{\partial r} + \frac{1}{r^2}\frac{\partial^2\Phi_0}{\partial\theta^2} = 0, \tag{6}$$

$$\frac{\partial^2\Phi_1}{\partial r^2} + \frac{1}{r}\frac{\partial\Phi_1}{\partial r} + \frac{1}{r^2}\frac{\partial^2\Phi_1}{\partial\theta^2} = -\frac{\partial^2\Phi_0}{\partial\hat{z}^2}. \tag{7}$$

The solution to Eq. (6) is obtained from the complex velocity potential, $f_i = \mu\left(ze^{-i\omega_i t} + e^{i\omega_i t}/z\right)\sin\alpha(z)$, of the doublet with the strength, $\mu = Q_L\Delta s/(4\pi)$. We note that the lateral displacement of the jet, $\alpha(z)$, is given by Madarame et al. (2002). Assuming that $\alpha(z) \prec 1$, the complex velocity potential becomes approximately $f_i = \mu\alpha(z)\left(ze^{-i\omega_i t} + e^{i\omega_i t}/z\right)$ and then the first-order solution, $\Phi_0$, is written as

$$\Phi_0 = \mu\left(\frac{r}{a} + \frac{a}{r}\right)\alpha(z)\cos(\theta - \omega_i t). \tag{8}$$

Substituting Eq. (8) into Eq. (7), Eq. (7) becomes

$$\left(\frac{\partial^2}{\partial r^2} + \frac{1}{r}\frac{\partial}{\partial r} + \frac{1}{r^2}\frac{\partial^2}{\partial\theta^2}\right)\Phi_1 = -\mu\left(\frac{r}{a} + \frac{a}{r}\right)\frac{\mathrm{d}^2\alpha(\hat{z})}{\mathrm{d}\hat{z}^2}\cos(\theta - \omega_i t). \tag{9}$$

The solution to Eq. (9) is then obtained as, with satisfying the rigid boundary condition,

$$\Phi_1 = -\mu\left[\frac{3}{8a}\left(r^3 - a^2 r\right) + \frac{a}{2}r\log\frac{r}{a} - \frac{a}{2}r\right]\frac{\mathrm{d}^2\alpha(\hat{z})}{\mathrm{d}\hat{z}^2}\cos(\theta - \omega_i t). \tag{10}$$

Combining Eqs. (8) and (10), the second-order solution is obtained as

$$\Phi(r,\theta,\hat{z};t) \approx \mu\left(\frac{r}{a} + \frac{a}{r}\right)\alpha(\hat{z})\cos(\theta - \omega_i t) - \mu\left[\frac{3}{8a}\left(r^3 - a^2 r\right) + \frac{a}{2}r\log\frac{r}{a} - \frac{a}{2}r\right]\frac{\mathrm{d}^2\alpha(\hat{z})}{\mathrm{d}\hat{z}^2}\cos(\theta - \omega_i t), \tag{11}$$

where the derivative of $\alpha(\hat{z})$ is calculated by using Eqs. (3)-(8) of Madarame et al. (2002). Total tangential velocity, $u_\theta = u_\theta^s + (1/r)(\partial\Phi/\partial\theta) := u_\theta^s + u_\theta^j$, is calculated by differentiating Eq. (11) with respect to $\theta$ and the numerical estimation is listed in Table 1. As seen in this table, the inlet jet could affect the horizontal velocity field and, however, the contribution of Eq. (11), namely $|u_\theta^j|$, is sufficiently small compared with $|u_\theta^s|$. Therefore, the difference of the theoretical velocity, $u_\theta^s$, on the depression side is found to be caused by the assumption of the small amplitude. We finally notice that the inlet jet model of Eq. (11) does not take into account the effects of the boundary layer, the dissipation of the turbulence and the free surface swell due to the inlet jet.

# 5. Conclusions

Jet-induced rotary sloshing of a Newtonian fluid in a partially filled cylindrical container has been visualized to investigate a flow pattern inside the rotary sloshing wave. Visualization techniques employed in this study have been included in Computational Fluid Dynamics (CFD) based upon the full Navier-Stokes equations and Particle Image Velocimetry (PIV).

A swirl period for the various aspect ratios was computed and experimentally measured, and tested against the theoretical result of the small time-harmonic irrotational sloshing of an inviscid, incompressible fluid. Results for $\mathscr{A} = 0.5$ and $Q_L = 2.6 \times 10^{-4}$ m$^3$/s have been given. Experimental result of the coloured inlet jet was virtually identical with the theoretical model of the jet streakline of Madarame et al. (2002). In the selected comparison of the flow patterns between the CFD and PIV results, each result was virtually identical for the 3D view and in nice agreement for the amplitude of the sloshing and the velocity vector in the vertical and horizontal cross-sections. In the jet-induced rotary sloshing, the pure inviscid sloshing solution of Eqs. (2)-(4) is dominant except for the core region of the inlet jet. In addition, a physical model of

the inlet jet, $u_\theta^j$, was proposed and the tangential velocity due to the inlet jet was estimated. The effect of the inlet jet was then found to be sufficiently small compared with the velocity field of the rotary sloshing except for the core region of the inlet jet. However, the physical model of the inlet jet, Eq. (11), introduced in this paper was based upon the potential flow theory and, therefore, the effects of the boundary layer, turbulence and the free surface swell due to the inlet jet could not be clearly estimated. Indeed, the CFD and PIV results exhibited that the horizontal velocity is slightly weaker on the elevation side than on the depression side.

## *References*

Cortelezzi, L. and Karagozian, A. R., On the formulation of the counter-rotating vortex pair in transverse jets, J. Fluid Mech., 446 (2001), 347-373.
FLUENT 6.2 User's Guide, (2005), Fluent Inc., Lebanon, NH.
Ibrahim, R. A., Liquid Sloshing Dynamics, (2005), 12-16, Cambridge University Press.
Iguchi, M., Sasaki, Y., Sasaki, K. and Yoshida, J., Design of Snow Melting Bath Agitated by Swirl Motion of Bubbling Jet, Jpn J. Multiphase Flow, 16-3 (2002), 232-239.
Lamb, H., Hydrodynamics, 6th edn, (1932), 282-307, Cambridge University Press.
Madarame, H., Okamoto, K. and Iida, M., Self-Induced Sloshing Caused by an Upward Round Jet Impinging on the Free Surface, J. Fluids and Structures, 16-3 (2002), 417-433.
Pozrikidis, C., Introduction to Theoretical and Computational Fluid Dynamics, (1997), 83-88, Oxford University Press.
Ramesh, G., Venkatakrishnan, L. and Prabhu, A., PIV Studies of Large Scale Structures in the Near Field of Small Aspect Ratio Elliptic Jets, J. Visualization, 9-1 (2006), 23-30.
Shitara, M., Iguchi, M., Takano, K., Tamamori, T., Shitara, H. and Maruyama, T., Processing of Refractory Organic Waste Water Using Ozone and Novel Agitation Method, Materials Transactions, 44-12 (2003), 2456-2460.
Ueda, Y., Hayashida, Y. and Iguchi, M., A Damping Wave of Jet-Induced Rotary Sloshing in a Cylindrical Container, Submitted to Trans. JSME (B).
Yoshida, J., Iguchi, D., Shitara, M. and Iguchi, M., Proposal of a Novel Agitation Method Using Swirl Motion of Molten Metal Jet, ISIJ International, 43-12 (2003), 1890-1896.
Watanabe, Y., Hashizume, Y. and Fujisawa, N., Simultaneous Flow Visualization and PIV Measurement of Turbulent Buoyant Plume, J. Visualization, 8-4 (2005), 293-294.

## *Author Profile*

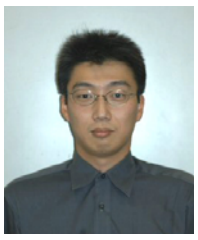

Yoshiaki Ueda: He received his Ph.D. in 2003 from Department of Mechanical Engineering at Osaka Prefecture University. He has been a visiting researcher in Laboratoire d'Hydrodynamique (LadHyX) at École Polytechnique, France (2004-2005). He is currently a Research Fellow of Japan Society for Promotion of Science (JSPS) in Department of Materials Science and Engineering at Hokkaido University. His research interests include: Low-Reynolds-Number Flow, Matched Asymptotic Expansions, Singular Integral Equation, Vortex Method and Jet-Induced Sloshing.

Yuuna Hayashida: He received his B.Sc. in 2005 from Department of Materials Science and Engineering at Hokkaido University. He is currently a graduate student (M.Sc. degree) in Department of Materials Science and Engineering at Hokkaido University. His research interests include: Flow Visualization, Jet-Induced Sloshing, Mixing, Steelmaking and Refining.

Manabu Iguchi: He received his M.Sc. (Eng.) in Mechanical Engineering in 1973 from Osaka University. He also received his Ph.D. in Mechanical Engineering in 1981 from Osaka University. He works in Division of Materials Science and Engineering, Graduate School of Engineering of Hokkaido University as a professor since 1996. His research interests are transport phenomena in materials processing operations and development of velocimeters for molten metals at high temperatures.

Toshio Ishii: He received his M.Sc. (Eng) in Mechanical Engineering in 1982 from Waseda University. He also received his Ph.D. in Mechanical Engineering in 2002 from Hokkaido University. He works as General Manager for Numerical Simulation Dept. and visiting professor at Hokkaido University. His research interests are multi-phase flow in steel process and development of new process for high quality steel product.